Optics and Laser Technology 109 (2019) 608–615

Contents lists available at ScienceDirect

Optics and Laser Technology

journal homepage: www.elsevier.com/locate/optlastec

Full length article

Fracture mechanisms in the as-built and stress-relieved laser powder bed fusion Ti6Al4V ELI alloy

A.M. Vilardell[a,*], G. Fredriksson[a], I. Yadroitsev[b], P. Krakhmalev[a]

[a] Karlstad University, Department of Engineering and Physics, Karlstad SE-651 88, Sweden
[b] Central University of Technology, Free State, Department of Mechanical and Mechatronic Engineering, Private Bag X20539, Bloemfontein 9300, South Africa

HIGHLIGHTS

- As-built LPBF Ti6Al4V ELI specimens have a fully martensitic microstructure.
- Stress-relief leads to a coarsening of needles and precipitations. No β-phase was observed.
- Ductile fracture mode dominated at impact test. Crack initiated earlier after stress relief.
- Multiple fatigue crack initiation due to surface roughness was observed.
- Crack propagation rate was slightly higher after stress relief.

ARTICLE INFO

Keywords:
Laser powder bed fusion
Ti6A4V ELI
Impact and fatigue properties
Stress-relief treatment
Fracture analysis

ABSTRACT

The influence of a stress-relief treatment on impact and fatigue properties of Ti6Al4V ELI samples manufactured by laser powder bed fusion was analyzed. The heat treatment resulted in removal of residual stresses, coarsening of needles and formation of precipitations between needles. In both, impact and fatigue tests, crack development was correlated to microstructural features. Fracture analysis was carried out by means of optical and electron microscopy to reveal the influence of microstructure on crack development. Ductile fracture was the dominating fracture mode at impact testing. Pore formation and coalescence were the main crack formation mechanisms. The microstructural changes led to a decrease in impact toughness after heat treatment. Presumably, this was a result of the precipitations between needles. Fatigue results showed multiple crack nucleation at the surface in both, as-built and stress-relieved material. The crack propagation rate was slightly higher and the crack was less deflected in the stress-relieved material due to the stress relief and coarsening of the microstructure.

1. Introduction

Laser powder bed fusion (LPBF) is an additive manufacturing (AM) process in which a high power laser beam melts metal powder and deposits it layer by layer to produce customized parts. Multiple, rapid heating-melting-solidification cycles build the material, while non-melted powder remains in place to support the structure. LPBF is a process that opens up opportunities for producing lightweight components with complex geometries and internal structures, which cannot be produced by conventional techniques [1]. The ability to produce near net shape parts with up to 99.9 % relative density is of great interest for the aerospace and automotive fields, and the ability to produce porous structures is of interest for biomedical purposes (e.g. scaffolds) [2].

Ti6Al4V is a low-density alloy that possesses a good combination of strength, toughness and corrosion resistance. It is a suitable candidate for aerospace applications due to its high strength-to-weight ratio, and also for biomedical applications for its biocompatibility [3]. This material is relatively easy to print with high density and therefore it attracts huge attention within the AM community. Conventional mechanical characteristics of LPBF Ti6Al4V were reported many times in as-built, and heat treated conditions [4,5]. Usually, the high cooling rates during LPBF (about 10^6 K/s) lead to the formation of α′-martensite, which promotes higher strength but gives less ductility [6]. Simonelli et al. [4] observed that a post heat treatment (730 °C during 2 h) lead to the transformation of α′-martensite → α + β phases, thus making slip transfer across the α/β interface possible and increasing the overall ductility. Vracken et al. [5] reported an increase of the ductility of LPBF specimens after a post heat treatment at 850 °C for 2 h up to 12.84 ± 1.36 % in comparison with 7.36 ± 1.32 % of the non-treated specimens.

---

* Corresponding author.
E-mail address: amvilardell.research@gmail.com (A.M. Vilardell).

https://doi.org/10.1016/j.optlastec.2018.08.042
Received 7 June 2018; Received in revised form 17 August 2018; Accepted 21 August 2018

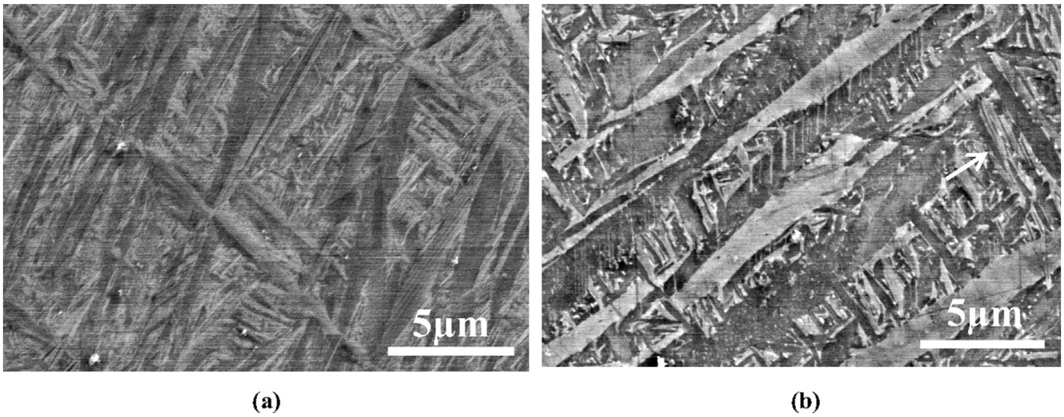

Fig. 1. SEM micrographs in backscattered electron mode of (a) AB and (b) SR LPBF Ti6Al4V ELI specimens.

Recently, new studies have been performed with a Ti6Al4V ELI (Extra Low Interstitial) alloy with less oxygen content, as this improves ductility, fracture toughness, stress-corrosion resistance and resistance against crack growth [7–9]. Those studies have demonstrated the feasibility of LPBF Ti6Al4V and ELI alloys, by achieving mechanical properties similar to components obtained by conventional processes [10].

It is known that one of the major causes of mechanical failure of engineering components is crack nucleation and propagation. In titanium alloys, a strong influence of microstructure on crack behavior has been reported [11]. Many investigations of AM Ti6Al4V have focused on the fatigue performance of LPBF Ti6Al4V material. They have presented an influence of surface roughness, porosity, surface finish and heat treatment on fatigue life [12]. Fewer publications have studied impact behavior of LPBF Ti6Al4V [13,14]. Nevertheless, in order to understand the durability of the material, it is of highest importance to understand how crack propagates under fatigue or impact conditions and to understand how cracks interact with the microstructure. This will give an input to the development of new heat-treatment procedures, providing tailored microstructures and predictable crack behavior for LPBF Ti6Al4V materials in demanding applications.

The present study presents results of impact and fatigue tests of LPBF Ti6Al4V ELI in as-built and stress-relieved conditions. The microstructure of the materials was investigated by means of electron microscopy including electron backscatter diffraction. The main focus was to understand fracture mechanisms and the interaction of cracks with microstructure.

2. Materials and methods

Ti6Al4V ELI alloy feedstock powder from TLS Technik GmbH & Co Spezialpulver KG was used to print the specimens. The powder showed a spherical morphology, typical for the gas atomization process. According to the manufacturing specification, the particle size was $d_{10} = 11.16\,\mu m$, $d_{50} = 20.64\,\mu m$, $d_{90} = 31.84\,\mu m$ (weighted by volume). Before manufacturing, the powder was dried at 80 °C for 2 h.

Specimens were produced by EOSINT M280 system (EOS GmbH) with volume rate $5\,mm^3/s$ for 30 μm powder layer thickness. Parameters recommended by the equipment producer were used for manufacturing of specimens. A back-and-forth (zigzag) scanning strategy by strips of 10 mm in width with a hatch distance of 100 μm was applied. All specimens, $10x10x60\,mm^3$ in size, were built without supports, directly on substrates of Ti6Al4V ELI. The long axis of the specimens was parallel to the building direction. Argon was used as protective atmosphere. The oxygen level in the chamber was controlled and it was in the range of 0.07–0.12 %. The stress-relief treatment was performed in a regular heat-treatment furnace at 650 °C during 3 h with a heating rate of 3.3 °C/min, followed by a furnace cooling. The furnace was equipped with a stainless steel box, continuously filled with Ar during the treatment. After the stress-relief treatment, the specimens were cut off from the substrate. Both, as-built (AB) and stress relieved (SR) specimens, were manufactured for impact and fatigue testing.

Charpy impact tests of un-notched specimens were performed with a Pendulum Impact Tester RKP 450 from Zwick/Roell in order to determine the toughness of the materials. The area under the force-displacement curve defines the energy absorbed by the test piece. All surfaces were grinded with 320 SiC paper. Three-point bending fatigue tests were carried out with an Instron 8801 equipment until failure. The stress amplitude was 700 MPa, the stress ratio $R = 0.1$ and the frequency 10 Hz. The most loaded surface of the specimens was left as-built, in order to study the influence of roughness. The surface roughness (R_a parameter) was measured by optical profiler ContourGT-K (Bruker). The other faces of the specimens were polished. Both tests were arranged so that the crack propagated perpendicular to the building direction i.e. perpendicular to the prior β-phase grains. The analysis of fracture surfaces was carried out in scanning electron microscope (SEM) LEO 1350 FEG, operated at 20 kV.

The microstructure of as-built and stress-relived materials was analyzed. Cross-sections were prepared by standard metallographic procedure. Samples were grinded up to 4000 SiC paper, polished with colloidal silica, and etched in Krolĺ's reagent for microstructural investigations. SEM and optical microscopy (Leica DMI 3000 M) were used for that purpose. Control of SEM and measurements of needle size were carried out by using SmartSEM® V05.04 SEM software provided by Carl Zeiss NTS GmbH.

3. Results

3.1. Microstructure analysis

Fig. 1a and b shows the needle microstructure of AB and SR materials, respectively. After the SR treatment, an increase in size of the martensitic needles can be observed. The average thickness of the needles was measured to be of 0.4 μm and 1.1 μm for AB and SR specimens, respectively. Additionally, the microstructure has changed. After SR treatment spot like precipitations between the needles appeared, but EBSD did not show any evidence of β-phase (Fig. 2).

3.2. Impact test

The characteristic force-displacement curves of each specimen are shown in Fig. 3. After sever plastic deformation, crack initiation and crack arrest points can be differentiated according to the standard specification ISO 14556 [15]. The energy absorbed by the material during the impact is described as the area under the force-displacement curve.

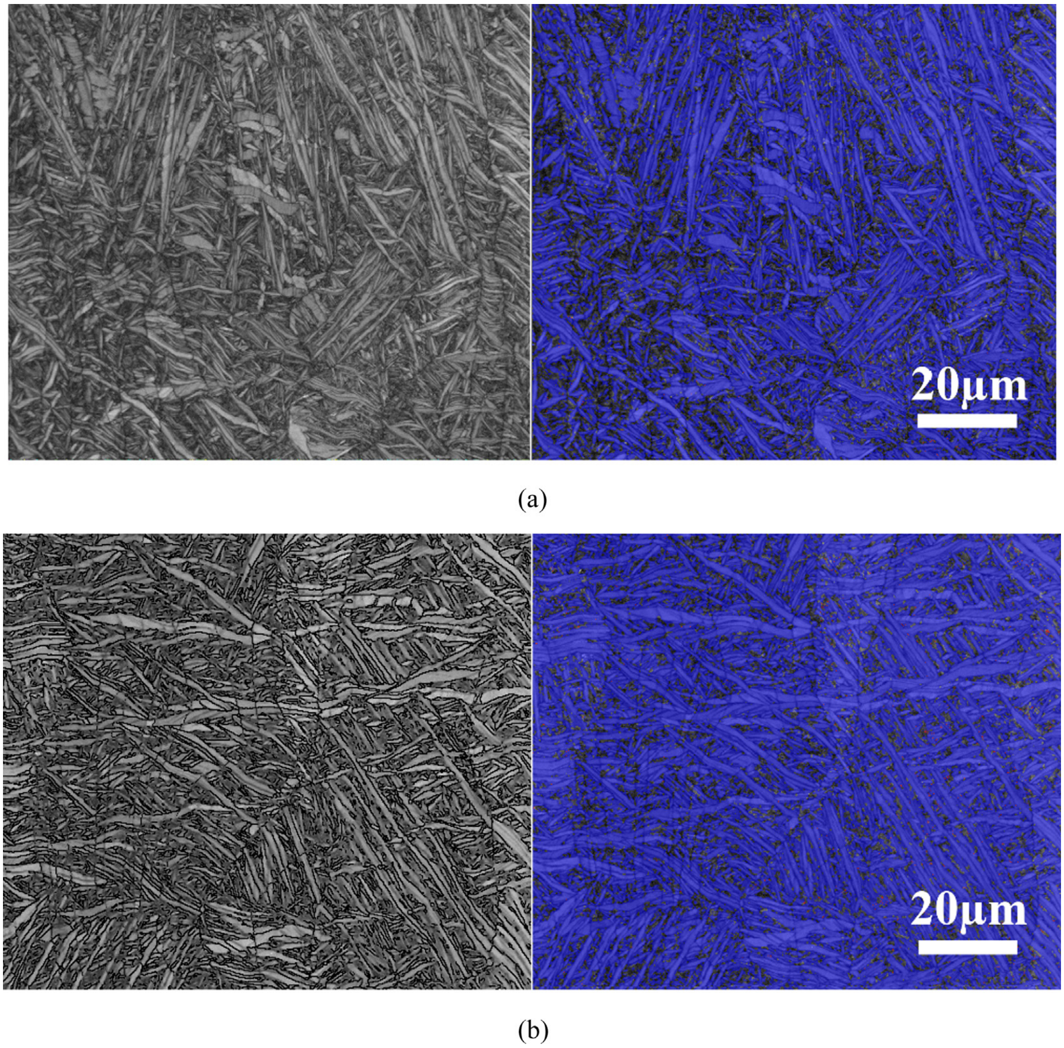

Fig. 2. EBSD results showing band contrast (left) and phase contrast (right) micrographs of (a) AB and (b) SR samples. (α/α′-phase: blue color; β-phase: red color). (For interpretation of the references to color in this figure legend, the reader is referred to the web version of this article).

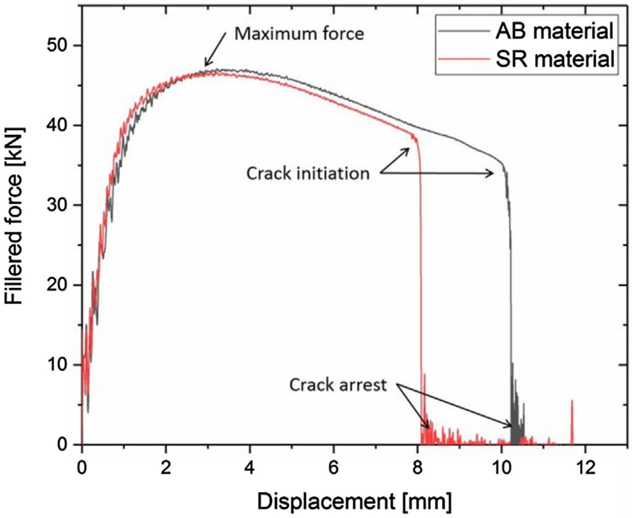

Fig. 3. Force-displacement curves of vertical AB and SR LPBF Ti6Al4V ELI specimens.

Table 1
Average values of force, displacement and energy parameters obtained by impact test.

Parameters	AB specimens	SR specimens
Force [kN]		
Maximum force (F_m)	47.5 ± 0.6	46.7 ± 0.0
Crack initiation force (F_{iu})	34.5 ± 0.8	38 ± 0.6
Crack arresting force (F_a)	13.3 ± 4.4	8 ± 1.1
Displacement [mm]		
Displacement at maximum force (S_m)	3.2 ± 0.1	3 ± 0.1
Crack initiation displacement (S_{iu})	10.2 ± 0.2	8 ± 0.1
Crack arresting displacement (S_a)	10.3 ± 0.1	8.2 ± 0.0
Energy [J]		
Energy at maximum force (W_m)	121.2 ± 1.1	115.6 ± 3.9
Crack initiation energy (W_{iu})	416.3 ± 8.8	332.0 ± 3.7
Crack arresting energy (W_a)	420.6 ± 6.2	336 ± 1.9

Table 1 shows the force and displacement values, as well as the absorbed energy during the impact at crack initiation and arresting points. The results show that the SR material absorbs less energy before crack initiation (W_{iu} = 332 J) than the AB material (W_{iu} = 416.3 J),

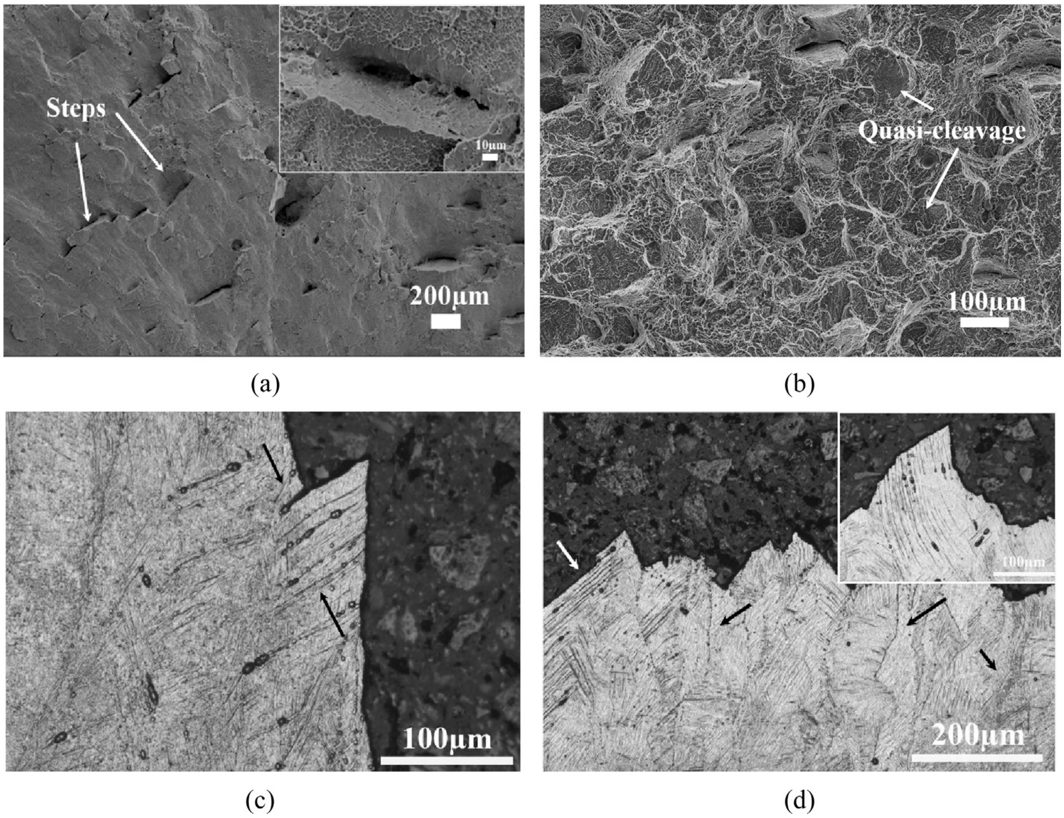

(a)
(b)
(c)
(d)

Fig. 4. SEM micrographs of fracture surface morphology of (a) the crack initiation region (typical steps are marked with arrows and shown in the inset) and (b) the crack propagation region (quasi-cleavage regions are marked with arrows); (c, d) optical micrographs of cross-sections: (c) corresponding to (a), and (d) corresponding to (b). The black arrows indicate the formation and coalescence of pore (c) between needles and (d) at prior β grain boundaries. The white arrows indicate the quasi-cleavage regions from Fig. 4b.

thus reaching higher displacement due to higher plastic deformation. Although both materials show a crack arresting point, the curves mainly show an unstable crack propagation by having similar crack initiation and crack arresting energy values.

The fracture surfaces after impact test of all specimens are similar in appearance. The proportion of ductile fracture surface was able to be calculated with the force values (Table 1) following Eq. (1) [15]. The results show 100 % and 95 % of ductile fracture surface for AB and SR specimens, respectively. It was an unexpected result since a brittle behavior due to martensitic microstructure was expected.

$$Ductile\ \ fracture\ (\%) = \left[1 - \frac{Fiu - Fa}{Fm}\right] \times 100\% \tag{1}$$

In all cases, an area with high plastic deformation where the crack initiated, a fibrous zone where the crack propagated, and shear lips were observed. Fig. 4 shows SEM micrographs of the fracture surface regions of crack initiation (Fig. 4a), and crack propagation (Fig. 4b). In the region of crack initiation, severe plastic deformation, shallow dimples and coalescence of voids was observed. Formation and coalescence of micro-voids lead to the formation of "terraces" clearly visible in Fig. 4a, indicated by arrows. Micro-dimples indicate ductile fracture. Fig. 4b shows a SEM micrograph of the fracture surface in the crack propagation region. The fracture surfaces of both AB and SR specimens have a similar appearance and the same features were observed. In both cases, "terrace" features were found. This could be a result of quasi-cleavage fracture [4] due to an interaction of the crack with features of the microstructure.

Fig. 4c and d shows the cross-sections of the fracture surfaces of Fig. 4a and b, respectively. The formation and coalescence of pores at prior β grain boundaries (Fig. 4d) and between needles (Fig. 4c and d) can be observed. The propagation of the crack along the needles led to the formation of the flat regions known as quasi-cleavage in Fig. 4d.

3.3. Fatigue test

Both, AB and SR specimens, were tested under three-point bending fatigue conditions and showed crack nucleation at the surface, which is not a surprise as the most loaded surface was left unpolished. Surface roughness values measured with optical profiler was $R_a = 18.0 \pm 0.1$ μm. Previous research on specimens from the same batch have shown that the fatigue life under bending of vertically built specimens increased about three times after stress-relief treatment [9]. Fig. 5a and b shows morphology of the most loaded surface of AB and SR specimens after failure. On the top surface close to the fracture surface of AB specimens, a number of secondary cracks parallel to the fracture surface can be observed. Less amounts of similar secondary cracks were observed on the top surface of the SR specimens.

Both specimens show multiple crack nucleation (Fig. 6a and b). Additionally, cracks were found to initiate in parallel planes, thus merging and creating irregular fracture paths seen from the top surface (Fig. 6a and b). The crack propagation areas show irregular surfaces composed by dimples and quasi-cleavage features on both AB and SR specimens (Fig. 6c).

To investigate the interaction of the main crack with the microstructure, vertical cross-sections were made parallel to the crack propagation direction, as close as possible to the location of the main crack (Fig. 7), see dashed lines in Fig. 6. Observations of several cross-sections showed that the fracture surface in the crack growth area was smoother in the SR specimens than in the AB ones.

Crack propagation was estimated based on electron microscopy observations of the width of striations on the fracture surfaces in dependence on the crack length (Fig. 8a). The calculations of ΔK value

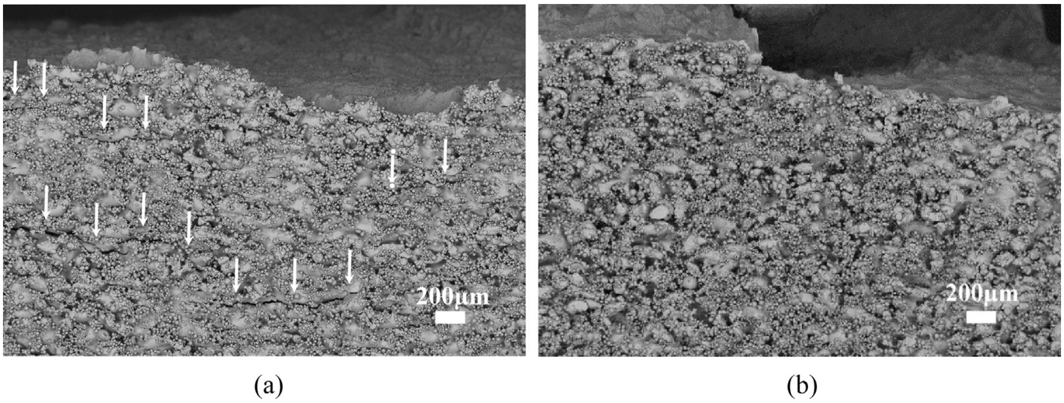

Fig. 5. Top surface areas of (a) AB and (b) SR specimens (Cracks indicated with white arrows).

were performed according to [16], based on the stress-intensity factor equations for semi-elliptical surface crack model. The crack growth data (da/dN) obtained from measurements on the fracture surface was plotted versus the calculated stress intensity range (ΔK), and Pariś law (Eq. (2)) was used to estimate values for the material parameters C and m.

$$\frac{da}{dN} = C(\Delta K)^m \tag{2}$$

Fig. 8b shows the typical behavior of crack growth. The sigmoidal curves can be divided into three different regions, usually known as I, II and III (inset Fig. 8b). Within region I (where stress levels are low and/or the length of the cracks are small), the pre-existing cracks will not grow with the cyclic loads. In other words, there exist a threshold value (ΔK_{TH}) below which fatigue cracks will not propagate. Above the threshold value there is a linear region (regime II) in Fig. 8b until the fracture toughness value (K_{IC}) is reached and final fracture occurs. The threshold value was found to be between K_{TH} = 4–7 MPa m$^{-1/2}$, and the fracture toughness K_{IC} = 25–30 MPa m$^{-1/2}$. The slope of the linear curve in regime II or the "m" value, was fitted to m = 1.32–1.45 (AB specimen) and 1.37–1.58 (SR specimen), which suggests that crack growth is slightly faster in SR than in AB specimens.

4. Discussion

Post heat treatments are commonly used to improve ductility, although strength can be reduced [5,17]. According to previously reported data, the stress-relief treatment of LPBF Ti6Al4V ELI material did not have any significant influence on yield strength, tensile strength or elastic modulus, but increased the elongation from 9.4 to 10.9 %, in comparison with AB specimens [8]. However, other mechanical properties such as impact toughness and fatigue needs to be understood for industrial applications. After the stress-relief treatment used in this study, the specimens did not show any remarkable microstructural

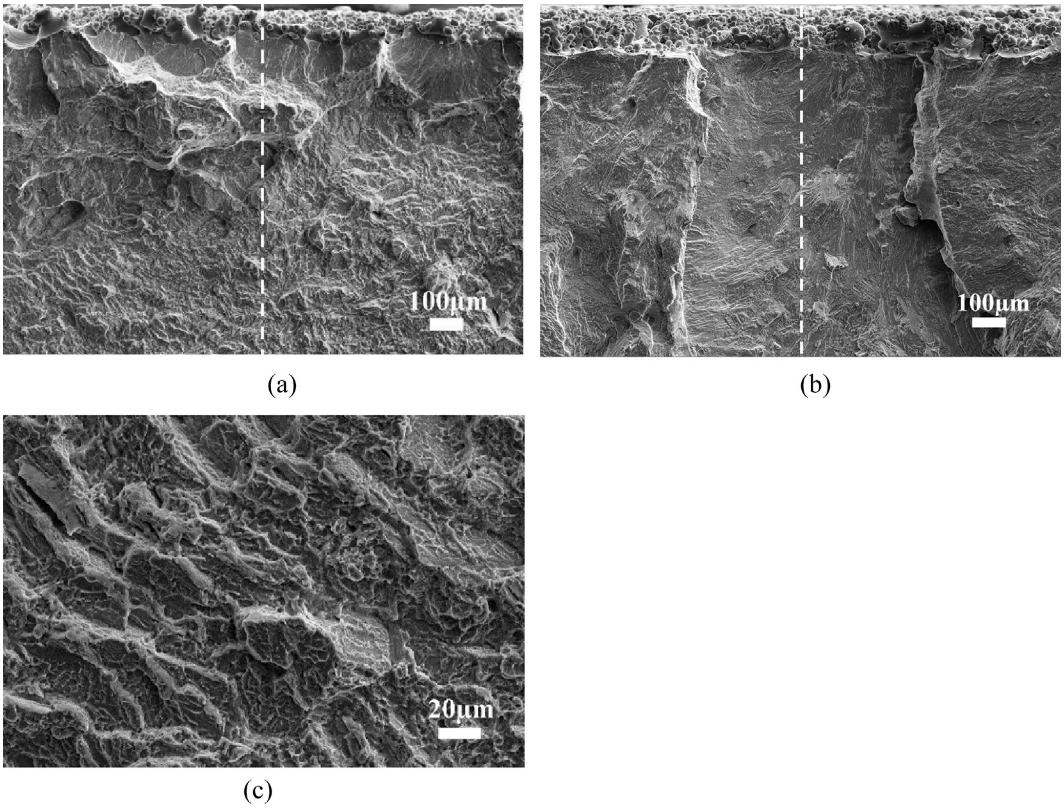

Fig. 6. SEM micrographs of crack initiation (a, b) and propagation (c) regions. The dashed line illustrates the direction of the cross-sections (in Fig. 7).

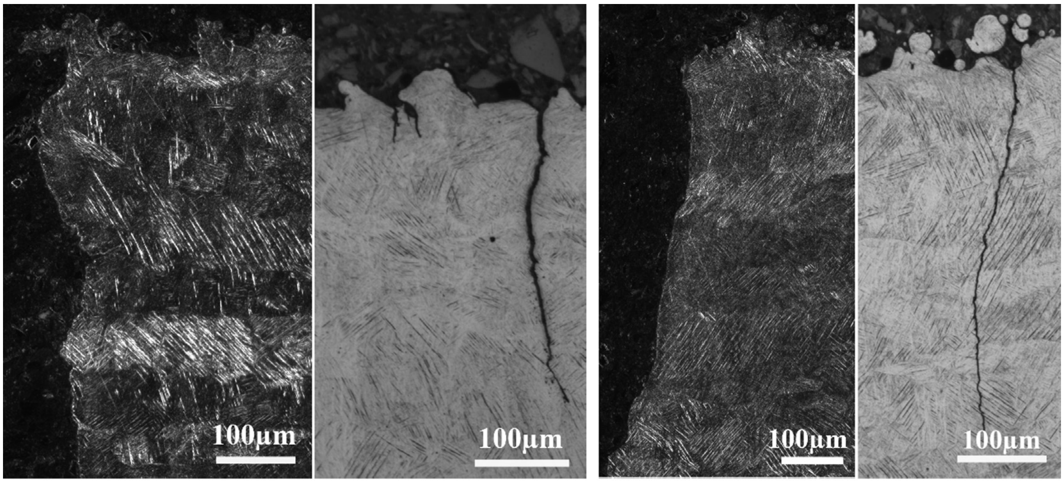

(a)

(b)

Fig. 7. Cross-section of (a) AB and (b) SR Ti6Al4V ELI fatigue specimens. Micrographs illustrate the main crack fracture and secondary cracks parallel to the main one.

changes. The needles still maintained the sharp morphology which is typical of the martensitic α′-phase. Since – α and α′ phases have HCP structure and quite similar lattice parameters, it is hard to distinguish them by XRD or EBSD. Commonly, they differ by needle morphology, in which more rounded shape needles correspond to the α-phase [18].

4.1. Impact testing

The effect of post heat treatments on mechanical properties of AM Ti6Al4V strongly depends on the initial α′-phase and its decomposition. Results obtained in the present investigation show that stress-relief treatment led to some decrease in the energy absorbed before crack initiation.

Commonly an improvement of impact toughness was reported for heat-treated LPBF specimens [13,14,19,20]. Wu et al. [19] attributed the improvement of impact toughness to the elimination of the disc-shaped pores and the transformation of α′-martensite into a lamellar α + β structure after HIP treatment (1000 °C/150 MPa). Meyer et al. [20] studied the effect of different aging treatments (1 h) on mill-annealed Ti6Al4V specimens, where temperatures for solution annealing and final aging as well as cooling rate were varied. From all conditions, those with α + β structures showed high impact toughness. In contrary, the results obtained in this study showed the opposite trend, which is consistent with the findings of Yasa et al. [13], who performed a heat treatment of 3 h at 595 °C.

Usually, in as-built conditions, the microstructure of LPBF Ti6Al4V consists of α′-martensite. The lack of ductility of the α-phase has resulted in the development of post heat treatments to homogenize the microstructure, release residual stresses and improve ductility with minimum loss in strength [21]. It has been reported that heat treatments carried out at temperatures of 440–590 °C result in residual stress relaxation [19,22], while those at 760–850 °C result in the decomposition of α′ into α + β phases [4,5]. However, α′ decompositions has been reported to start earlier (~400 °C) [22,23]. Currently, different changes of microstructures have been reported after stress-relief treatment: (i) the formation of very fine needles consisting completely of α-phase and α′-martensite (650 °C for 3 h) [24], (ii) partial decomposition of α′-martensite phase towards acicular α by slight coarsening of the microstructure (650 °C for 4 h) [19], and (iii) fine precipitation of β-phase along the α′ needle boundaries (650 °C for 2 h) [22].

In the present investigation, changes in morphology of the needles after stress-relief heat treatment were observed by electron and optical microscopy, Fig. 1a and b. The average thickness of the needles increased and small precipitates appeared between the needles. However, EBSD did not detect any β-phase (Fig. 2). Often, similar precipitations have been reported after heat treatment [19,22,24]. At the same time, small white precipitations between α/α′ needles were visible in the as-built specimens, but also in as-built specimens [25,26]. The precipitations found in as-built specimens were located between α/α′ needles and have been identified as α-phase, and called “α rods” and “α dots”

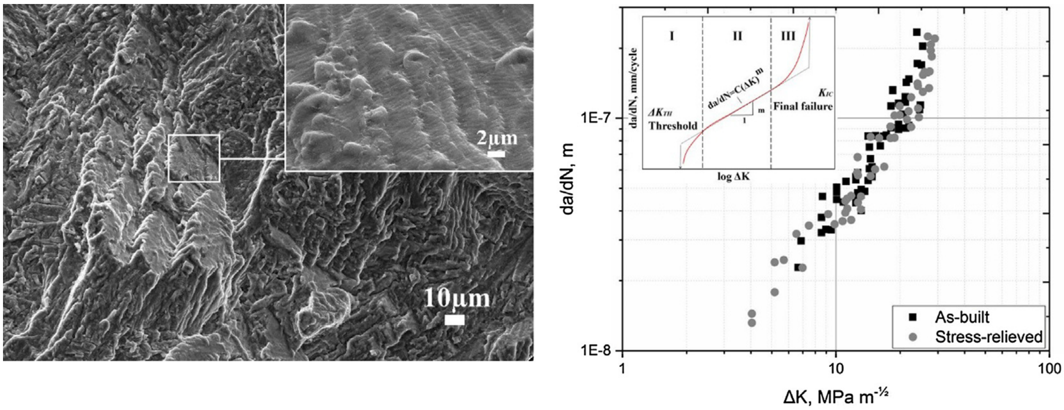

(a)

(b)

Fig. 8. (a) SEM micrograph of surface striations. (b) Fatigue crack propagation of AB and SR LPBF Ti6Al4V ELI specimens.

based on SEM and EDS analyses [25]. In another study, they were identified as primary α′, secondary α′, tertiary α′, quartic α′ and α rods and dots, Agius et al. [26]. The formation of these precipitates was associated with intrinsic low-temperature heat treatment during manufacturing [23,25,26]. Commonly, the presence of precipitation on interfaces can result in a decrease of toughness of the material. Therefore, the lower impact energy values observed in the SR material in this study, could be attributed to the presence of the precipitations observed by electron microscopy.

In the crack initiation area, the fracture surface has quite the same morphology for both AB and SR specimens. Coalescence of pores and formation and coalescence of new voids forming "terraces" are the main mechanisms of the crack initiation. In the crack development region, morphology of the fracture surface is also quite similar. Ductile fracture with formation of dimples was observed, Fig. 4a. Cross-sections of this region revealed a strong interaction of the crack with the microstructure. Fig. 4c and d shows the presence of micro-voids between the needles in the colony. The crack has a distinguished deflection on prior β grain boundaries and are strongly influenced by the orientation of the needles within the prior β grains. The presence of precipitates between needles in the SR specimens, may facilitate the formation of voids and accelerate crack nucleation. This can be an explanation to the experimentally observed difference in W_{iu} values between the AB and SR specimens (Table 1). Additionally, a coarsening of microstructure was observed (Fig. 1b). Zhang et al. [21] has shown a declining trend of ultimate compressive strength and yield strength with increasing temperature of the heat treatment, as well as with the coarsening of needles in LPBF Ti6Al4V material. In conventional Ti6Al4V with α + β microstructure, a high impact toughness has been reported [20]. In the present investigation, coarsening of the microstructure did not lead to an increase of toughness, possibly due to a negative effect of precipitations.

4.2. Fatigue behavior

The study of fatigue crack nucleation and propagation carried out in this investigation, showed that cracks nucleated at the surface due to surface roughness. Surface roughness is known to influence fatigue life of AM Ti6Al4V significantly. In the literature, it has been reported that machining of the surface increased fatigue life substantially, especially at low stress amplitudes [12]. The deepest valleys and notches at the as-built surface of the LPBF Ti6Al4V specimens play a role as stress concentrators. The random distribution of these surface defects led to multiple nucleation of sub-critical cracks. These cracks grew parallel to each other at the loaded surface, Fig. 7. When these sub-critical cracks reached a critical size, they merged, but as they were not nucleated in the same plane, the finally formed crack is characterized by deflections and irregularities, Fig. 6b.

In the AB specimens, the number of parallel cracks initiated during the test was high, Fig. 5a. In the SR specimens such parallel cracks were rarely observed (Fig. 5b). The difference could be explained by the relief of residual stresses in the SR specimens. Residual stresses are known to influence fatigue life of AM Ti6Al4V significantly. Studies reported that stress-relief treatment increased fatigue life by one order of magnitude [12]. Nevertheless, the final crack formed after the merging of sub-critical cracks is still irregular in the SR specimen as well. Although the stress was relieved, the surface roughness still led to multiple crack nucleation, which in turn resulted in deflections and irregularities at the fracture surface.

From the crack propagation curves, illustrated in Fig. 8b, it is clear that the crack propagation rate is quite similar in both SR and AB specimens. However, the coefficient m in Eq. (2) is slightly lower for the AB material (Fig. 8b). The m values are 1.32–1.45 in AB and 1.37–1.58 in SR. Similarly, higher fatigue crack propagation rates in SR specimens were observed in LPBF Ti6Al4V ELI [9]. The fracture surfaces of the AB specimens were rougher than those of the SR specimens, Fig. 7. Commonly, a more deflected crack propagation path indicates more energy dissipation, and therefore, a lower propagation rate. In AB material, the fatigue crack deflects at every prior beta boundary, often following the interface between the needles. This resulted in a tortuous crack path and formation of the typical terraces with quasi-cleavage morphology at the fracture surface seen in Fig. 6c. In the SR material, the crack grew straighter, with less significant deflection, although terraces were observed here also. The difference in behavior could be explained by the contribution of residual stresses. The residual stresses influence the stress state at the crack tip, which can result in local changes in crack propagation direction. Thus leading to a more significant crack deflection in the AB material.

Heat treatment usually improves fatigue properties of AM Ti6Al4V material remarkably. Leuders et al. [27] studied the crack growth of LPBF Ti6Al4V specimens in four different conditions: (i) AB, after a heat treatment at (ii) 800 °C and another at (iii) 1050 °C during 2 h each, and (iv) HIP treated. All post heat treatments resulted in a significant increase in mean fatigue life and threshold values for crack propagation. Similar results have been obtained by Cain et al. [18] who studied fracture toughness and crack propagation of as-built, stress relieved (650 °C for 4 h) and heat treated (890 °C for 2 h) specimens in different specimen orientations. They found that the post heat treatments improved both fracture toughness and crack growth resistance. The stress-relief heat treatment used in the present study did not show as significant influence on threshold values and crack propagation rates as has been reported [18,27]. In those investigations, the heat-treatment were performed at higer temperatures and for longer times. This heat treatments changed microstructure, thus leading to more significant changes in the influcence of crack propagation rates compared to the present study. Only slight changes in microstructure, such as coarsening of needles and formation of precipitates, were observed in SR specimens. These changes led a slightly higher crack growth rate in the SR material was observed. Usually, changes in fatigue properties after heat treatment are attributed to relief of residual stresses and changes in microstructure, coarsening of needles and formation of β-phase. Coarsening of needles has been reported by others to decrease fatigue crack propagation rates in conventional Ti6Al4V material [11]. Coarsening of needles and relief of residual stresses, therefore can be considered as the main factors influencing the fatigue crack propagation rate. The microstructural changes observed in this investigation did not seem to influence the nucleation of fatigue cracks at bending fatigue test. Nucleation was rather governed by surface roughness and residual stresses. In both, AB and SR materials multiple crack nucleation was observed, but the number of cracks were higher in the AB specimens.

5. Conclusions

Microstructural characterization as well as impact and bending fatigue tests of LPBF Ti6Al4V ELI in as-built and stress-relieved conditions showed that:

- As-built LPBF Ti6Al4V ELI alloy specimens have a fully martensitic microstructure. The stress-relief treatment at 650 °C for 3 h leads to a coarsening of needles, and precipitations between needles. The needle width increased from 0.4 μm to 1.1 μm. β-phase was not detected by EBSD.
- The microstructural changes negatively influenced the impact properties, the crack initiation energy W_{iu} of the SR specimens was about 20 % lower than that of the AB specimens. It is suggested that crack nucleation by the formation and coalescence of micro-voids along the needles during impact was the main crack formation mechanism.
- Fatigue crack nucleation was observed at the rough surface. Stress relief reduced the number of parallel cracks initiated on the top surface. Still multiple crack nucleation and irregular shape were characteristics of the fracture surface in both AB and SR materials.

- The stress-relief treatment had a minor influence on the resistance to fatigue crack propagation. After stress relief, the crack propagation rate was slightly higher and the fracture surface in the crack growth area was smoother in SR specimens.

Acknowledgements

Authors thank the South African Research Chairs Initiative of the Department of Science and Technology and National Research Foundation of South Africa (Grant №97994), the Collaborative Program in Additive Manufacturing (Contract №CSIR-NLC-CPAM-15-MOA-CUT-01) and, the Swedish Agency for Economic and Regional Growth, (Grant №20201144). Ru Peng, Linköping University is greatly acknowledged for help with EBSD investigations and data analysis.

References

[1] C.Y. Yap, C.K. Chua, Z.L. Dong, Z.H. Liu, D.Q. Zhang, L.E. Loh, S.L. Sing, Review of selective laser melting: Materials and applications, Appl. Phys. Rev. 2 (2015) 041101, https://doi.org/10.1063/1.4935926.

[2] N. Guo, M.C. Leu, Additive manufacturing: technology, applications and research needs, Appl. Mach. Mater. 8 (2013) 215–243, https://doi.org/10.1007/s11465-013-0248-8.

[3] L.-C. Zhang, H. Attar, M. Calin, J. Eckert, Review on manufacture by selective laser melting and properties of titanium based materials for biomedical applications, Mater. Technol. 31 (2016) 66–76, https://doi.org/10.1179/1753555715Y.0000000076.

[4] M. Simonelli, Y.Y. Tse, C. Tuck, Effect of the build orientation on the mechanical properties and fracture modes of SLM Ti–6Al–4V, Mater. Sci. Eng. A-Struct. 616 (2014) 1–11, https://doi.org/10.1016/j.msea.2014.07.086.

[5] B. Vrancken, L. Thijs, J.-P. Kruth, J. Van Humbeeck, Heat treatment of Ti6Al4V produced by Selective Laser Melting: microstructure and mechanical properties, J. Alloy Compd. 541 (2012) 177–185, https://doi.org/10.1016/j.jallcom.2012.07.022.

[6] J. Zielinski, H.-W. Mindt, J. Düchting, J.H. Schleifenbaum, M. Megahed, Numerical and experimental study of Ti6Al4V components manufactured using powder bed fusion additive manufacturing, JOM 69 (2017) 2711–2718, https://doi.org/10.1007/s11837-017-2596-z.

[7] M.J. Donachie, Titanium: A Technical Guide, second ed., ASM International, Materials Park, Ohio, 2000.

[8] M.G. Moletsane, P. Krakhmalev, N. Kazantseva, A. du Plessis, I. Yadroitsava, I. Yadroitsev, Tensile properties and microstructure of direct metal laser-sintered Ti6Al4V (ELI) alloy, S. Afr. J. Ind. Eng. 27 (2016), https://doi.org/10.7166/27-3-1667.

[9] I. Yadroitsev, P. Krakhmalev, I. Yadroitsava, A. Du Plessis, Qualification of Ti6Al4V ELI alloy produced by laser powder bed fusion for biomedical applications, JOM. 70 (2018) 372–377, https://doi.org/10.1007/s11837-017-2655-5.

[10] V. Chastand, A. Tezenas, Y. Cadoret, P. Quaegebeur, W. Maia, E. Charkaluk, Fatigue characterization of Titanium Ti-6Al-4V samples produced by Additive Manufacturing, Procedia Struct. Integrity 2 (2016) 3168–3176, https://doi.org/10.1016/j.prostr.2016.06.395.

[11] G. Lütjering, J.C. Williams, A. Gysler, Microstructure and mechanical properties of titanium alloys, Microstructure and Properties of Materials, World Scientific, 2000, pp. 1–77, , https://doi.org/10.1142/9789812793959_0001 (accessed May 30, 2018).

[12] P. Li, D.H. Warner, A. Fatemi, N. Phan, Critical assessment of the fatigue performance of additively manufactured Ti–6Al–4V and perspective for future research, Int. J. Fatigue 85 (2016) 130–143, https://doi.org/10.1016/j.ijfatigue.2015.12.003.

[13] E. Yasa, J. Deckers, J.-P. Kruth, M. Rombouts, J. Luyten, Charpy impact testing of metallic selective laser melting parts, Virtual Phys Prototyp. 5 (2010) 89–98, https://doi.org/10.1080/17452751003703894.

[14] M.-W. Wu, P.-H. Lai, J.-K. Chen, Anisotropy in the impact toughness of selective laser melted Ti–6Al–4V alloy, Mater. Sci. Eng. A-Struct. 650 (2016) 295–299, https://doi.org/10.1016/j.msea.2015.10.045.

[15] Standard specification ISO 14556, Metallic Materials – Charpy V-Notch Pendulum Impact Test – Instrumented Test Method.

[16] J.C. Newman, I.S. Raju, Stress-Intensity Factor Equations for Cracks in Three-Dimensional Finite Bodies Subjected to Tension and Bending Loads: NASA Technical Memorandum 85793. NASA, Hampton, 1984.

[17] T. Vilaro, C. Colin, J.D. Bartout, As-fabricated and heat-treated microstructures of the Ti-6Al-4v alloy processed by selective laser melting, Metall. Mater. Trans. A. 42 (2011) 3190–3199, https://doi.org/10.1007/s11661-011-0731-y.

[18] V. Cain, L. Thijs, J. Van Humbeeck, B. Van Hooreweder, R. Knutsen, Crack propagation and fracture toughness of Ti6Al4V alloy produced by selective laser melting, Addit. Manuf. 5 (2015) 68–76, https://doi.org/10.1016/j.addma.2014.12.006.

[19] M.-W. Wu, P.-H. Lai, The positive effect of hot isostatic pressing on improving the anisotropies of bending and impact properties in selective laser melted Ti-6Al-4V alloy, Mater. Sci. Eng. A-Struct. 658 (2016) 429–438, https://doi.org/10.1016/j.msea.2016.02.023.

[20] L.W. Meyer, L. Krüger, K. Sommer, T. Halle, M. Hockauf, Dynamic strength and failure behavior of titanium alloy Ti-6Al-4V for a variation of heat treatments, Mech. Time-Depend. Mater. 12 (2008) 237–247, https://doi.org/10.1007/s11043-008-9060-y.

[21] X.-Y. Zhang, G. Fang, S. Leeflang, A.J. Böttger, A.A. Zadpoor, J. Zhou, Effect of subtransus heat treatment on the microstructure and mechanical properties of additively manufactured Ti-6Al-4V alloy, J. Alloy Compd. 735 (2018) 1562–1575, https://doi.org/10.1016/j.jallcom.2017.11.263.

[22] E. Sallica-Leva, R. Caram, A.L. Jardini, J.B. Fogagnolo, Ductility improvement due to martensite α′ decomposition in porous Ti–6Al–4V parts produced by selective laser melting for orthopedic implants, J. Mech. Behav. Biomed. 54 (2016) 149–158, https://doi.org/10.1016/j.jmbbm.2015.09.020.

[23] W. Xu, M. Brandt, S. Sun, J. Elambasseril, Q. Liu, K. Latham, K. Xia, M. Qian, Additive manufacturing of strong and ductile Ti–6Al–4V by selective laser melting via in situ martensite decomposition, Acta Mater. 85 (2015) 74–84, https://doi.org/10.1016/j.actamat.2014.11.028.

[24] E. Wycisk, S. Siddique, D. Herzog, F. Walther, C. Emmelmann, Fatigue performance of laser additive manufactured Ti–6Al–4V in very high cycle fatigue regime up to 10^9 cycles, Front Mater. 2 (2015), https://doi.org/10.3389/fmats.2015.00072.

[25] J. Lin, Y. Lv, Y. Liu, Z. Sun, K. Wang, Z. Li, Y. Wu, B. Xu, Microstructural evolution and mechanical property of Ti-6Al-4V wall deposited by continuous plasma arc additive manufacturing without post heat treatment, J. Mech. Behav. Biomed. 69 (2017) 19–29, https://doi.org/10.1016/j.jmbbm.2016.12.015.

[26] D. Agius, K.I. Kourousis, C. Wallbrink, T. Song, Cyclic plasticity and microstructure of as-built SLM Ti-6Al-4V: the effect of build orientation, Mater. Sci. Eng. A-Struct. 701 (2017) 85–100, https://doi.org/10.1016/j.msea.2017.06.069.

[27] S. Leuders, M. Thöne, A. Riemer, T. Niendorf, T. Tröster, H.A. Richard, H.J. Maier, On the mechanical behaviour of titanium alloy TiAl6V4 manufactured by selective laser melting: fatigue resistance and crack growth performance, I. J. Fatigue. 48 (2013) 300–307, https://doi.org/10.1016/j.ijfatigue.2012.11.011.